THE JOURNAL OF PHYSICAL CHEMISTRY C
A JOURNAL OF THE AMERICAN CHEMICAL SOCIETY

pubs.acs.org/JPCC
Article

Growth of NiO Thin Films in the Presence of Water Vapor: Insights from Experiments and Theory

Mattia Benedet, Chiara Maccato,* Gioele Pagot, Cristiano Invernizzi, Cinzia Sada, Vito Di Noto, Gian Andrea Rizzi, Ettore Fois, Gloria Tabacchi,* and Davide Barreca

Cite This: https://doi.org/10.1021/acs.jpcc.3c05067

ABSTRACT: NiO-based thin films and nanomaterials are promising candidates for a variety of end-uses, encompassing photo- and electrocatalysts, solar cells, displays, and sensors. This widespread attention has strongly fueled the interest in the fabrication of tailored systems featuring modular chemico-physical properties as a function of the required application. In this study, a single-step chemical vapor deposition (CVD) route for the preparation of pure and fluorine-doped NiO films is presented. Growth experiments were performed under water vapor-containing oxygen atmospheres from a series of Ni(II) β-diketonate−diamine molecular precursors featuring a different fluorination degree of the ligand side chain. A comprehensive experimental and theoretical investigation yielded valuable insights into the growth mechanism, with particular regard to the dependence of the system electronic properties on fluorine doping and content, and to the role exerted by water vapor in the reaction atmosphere. In fact, the interactions of water with the diketonate ligands contribute to weaken Ni−O bonds, favoring precursor activation. The obtainment of F-doped NiO systems from fluorinated derivatives and the simplicity of our process make the adopted strategy a valuable tool to control the system characteristics for a variety of eventual functional applications.

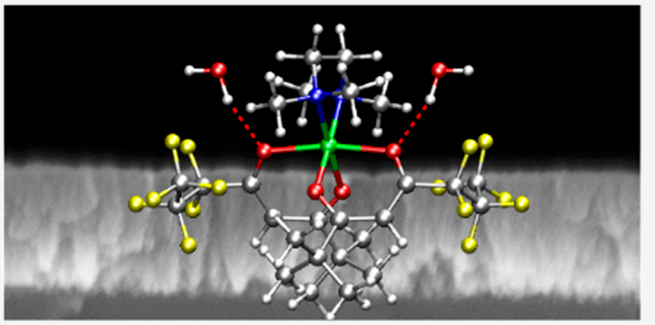

1. INTRODUCTION

The significant interest devoted to thin films and nanosystems based on NiO, a prototype p-type transparent semiconductor featuring a good chemical stability and a wide band gap (E_G = 3.2−4.0 eV),[1−5] can be traced back to their numerous important technological applications. The latter include resistive random access memories,[6−8] sensors,[3,9] hole extraction layers for solar cells,[2,5,10,11] displays, light-emitting diodes,[12] heterogeneous (photo)catalysts,[13,14] and electrocatalysts for the oxygen evolution reaction,[15−18] the bottleneck of H_2O splitting to yield clean hydrogen fuel. Overall, these applications directly benefit from high-quality film interfaces with the underlying substrate and from the obtainment of tailored NiO nanostructure, morphology, and chemical composition.[15] Because the latter and, hence, functional performances are strongly dependent on the adopted preparation strategy, supported NiO thin films/nanostructures have been fabricated by various physical and chemical routes, including sputtering,[1,3,19−23] molecular beam epitaxy,[24] electron beam evaporation,[4] spray pyrolysis,[25] spin coating,[2,5,11] hydrothermal synthesis,[14] atomic layer epitaxy,[26,27] atomic layer deposition,[6,7,28,29] and chemical vapor deposition (CVD).[10,15,16,30,31] In particular, the latter presents various concurrent advantages to control material features under non-equilibrium conditions by a suitable choice of experimental parameters and of the starting precursors.[32−36]

Recently, we have reported on the preparation and chemico-physical characterization of three β-diketonate−diamine Ni(II) adducts, *i.e.*, Ni(tfa)$_2$TMEDA, Ni(fod)$_2$TMEDA, and Ni(thd)$_2$TMEDA (Htfa = 1,1,1-trifluoro-2,4-pentanedione, Hfod = 2,2-dimethyl-6,6,7,7,8,8,8-heptafluoro-3,5-octanedione, Hthd = 2,2,6,6-tetramethyl-3,5-heptanedione, TMEDA = *N*,*N*,*N*′,*N*′-tetramethylethylenediamine, Figure 1), featuring promising properties as molecular precursors for the vapor phase deposition of NiO thin films.[37] Preliminary CVD validation experiments under conventional dry O_2 atmospheres yielded very thin deposits, indicating a limited decomposition efficiency of the used precursors. This behavior was particularly evident for fluorinated compounds, *i.e.*, Ni(tfa)$_2$TMEDA and Ni(fod)$_2$TMEDA, in spite of their better transport properties if compared to fluorine-free Ni(thd)$_2$TMEDA. These results prompted us to further investigate proper variations in the

Received: July 27, 2023
Revised: October 11, 2023
Accepted: October 19, 2023

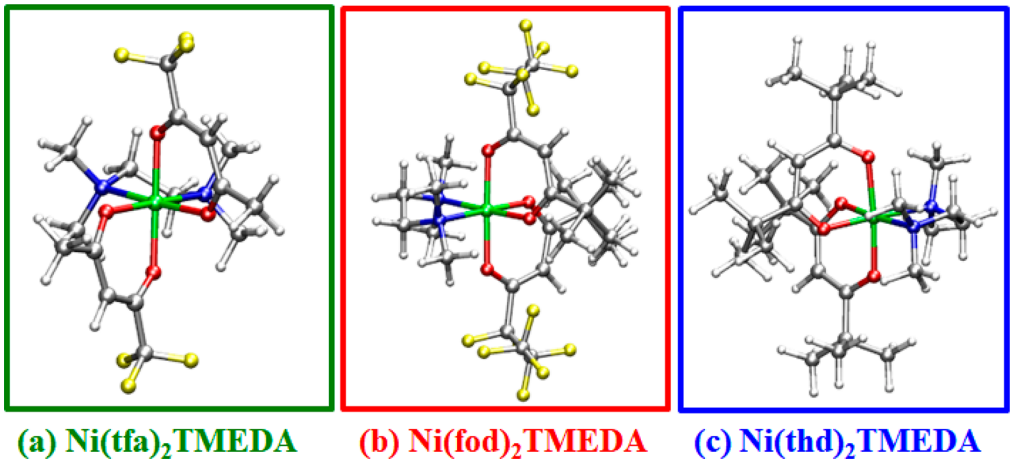

Figure 1. Sketch of the structures for $Ni(tfa)_2TMEDA$ (a), $Ni(fod)_2TMEDA$ (b), and $Ni(thd)_2TMEDA$ (c). Color codes: Ni, green; F, yellow; O, red; N, blue; C, gray; H, white.

growth conditions in order to optimize precursor conversion into the desired films, with particular regard to precursor−film property interrelations.

Previous works from our research group on the CVD of Fe_2O_3[33,38] and Co_3O_4[34,35] nanosystems have highlighted the effect exerted by the introduction of water vapor in the reaction atmosphere on both the thickness and the morphology of the obtained materials. On this basis, the present study focuses on the water vapor assisted-CVD of NiO films from the target precursors and on their subsequent chemico-physical characterization by a comprehensive set of advanced analytical techniques. The results provide evidence for the possibility of utilizing $Ni(tfa)_2TMEDA$ and $Ni(fod)_2TMEDA$ as single-source precursors for both Ni and F. To our knowledge, only a few examples of F-doped Ni oxide and hydroxide are available in the literature,[17,39,40] among which only one study on thin films,[39] and similar systems have never been obtained by CVD. The obtainment of F-doped NiO can indeed be a useful tool for a possible tailoring of material reactivity and optical/electrical characteristics in view of eventual optoelectronic, photocatalytic, and gas sensing end-uses.[39,41−44]

A further important advancement of the present study is provided by theoretical calculations, specifically aimed at elucidating the influence of water vapor on the precursor decomposition mechanism. These insights, which, to the best of our knowledge, have never been reported in the literature for similar systems, set the basis for a molecular understanding of oxide nanomaterial growth processes, which is of key relevance from both a fundamental and an applied point of view.

2. EXPERIMENTAL METHODS

2.1. Material Synthesis. NiO films were prepared by using a CVD custom-built horizontal cold wall reactor endowed with a quartz chamber and a resistively heated metal susceptor. Depositions were performed on pre-cleaned[38] 1 × 1 cm^2 Si(100) substrates (MEMC Electronic Materials S.p.A, Merano (BZ), Italy). In each run the used Ni precursor, synthesized as previously reported,[37] was heated in an external glass vessel at a suitable vaporization temperature [75, 80, and 120 °C for $Ni(tfa)_2TMEDA$, $Ni(fod)_2TMEDA$, and $Ni(thd)_2TMEDA$, respectively], and its vapors were transported into the reaction chamber by electronic grade O_2. An auxiliary O_2 flow was separately introduced into the reactor after passing through a water reservoir maintained at 35 °C. Flow rates [100 standard cubic centimeters per minute (sccm) for both the transport and auxiliary flow] were metered by MKS mass-flow controllers. All growth processes were performed at a total pressure of 10.0 mbar and at a substrate temperature of 400 °C.

2.2. Material Characterization. X-ray diffraction (XRD) measurements were performed by using a Bruker AXS D8 Advance Plus diffractometer equipped with a Göbel mirror, employing a Cu Kα X-ray source (40 kV, 40 mA). Crystallite sizes (D), dislocation density (δ), and microstrain (ε) values were calculated as reported in the Supporting Information (Section S2.1).

X-ray photoelectron spectroscopy (XPS), ultraviolet photoelectron spectroscopy (UPS), and reflection electron energy loss spectroscopy (REELS) analyses were performed by a ThermoFisher Scientific ESCALB QXi spectrometer. XPS measurements were performed by using a monochromatic Al Kα X-ray source ($h\nu$ = 1486.6 eV). Binding energies (BEs) were corrected for charging phenomena by attributing a value of 284.8 eV to the adventitious C 1s peak component (**I** in Figure S1). UPS analysis was performed by employing a He(I) ($h\nu$ = 21.22 eV) ultraviolet (UV) photon source generated by a helium plasma lamp. Work function measurements were taken with the sample biased at −3.0 V to further enhance the collection of the lowest kinetic energy electrons.[45,46] REELS analysis for band gap (E_G) measurements was performed with a primary electron beam energy of 1.0 keV. The measured energy band gap values were reproducible in repeated experiments (uncertainty = ±0.05 eV).

Secondary ion mass spectrometry (SIMS) measurements were performed by an IMS 4f instrument (Cameca), using a Cs^+ primary ion beam (14.5 keV, 30 nA; stability: 0.2%) and by negative secondary ion detection. Charge compensation was carried out by means of an electron gun. Analyses were conducted by rastering over a 150 × 150 μm^2 area, and collecting secondary ions from a sub-region close to 7 × 7 μm^2 to avoid crater effects. The erosion time was converted to depth using thickness values measured by field emission-scanning electron microscopy (FE-SEM).

https://doi.org/10.1021/acs.jpcc.3c05067
J. Phys. Chem. C XXXX, XXX, XXX−XXX

Atomic force microscopy (AFM) characterization was performed in air with an NT-MDT SPM Solver P47H-PRO instrument operated in tapping mode.

FE-SEM analyses were performed by means of a Zeiss SUPRA 40 VP apparatus, operating at primary electron beam voltages comprised between 10 and 20 kV. The mean nanoaggregate dimensions and deposit thickness values were estimated using the ImageJ software,[47] through a statistical image analysis.

2.3. Theoretical Calculations. The hydrated target compounds Ni(tfa)$_2$TMEDA, Ni(fod)$_2$TMEDA, and Ni(thd)$_2$TMEDA were theoretically studied within the density functional theory (DFT) framework, adopting the ωb97XD functional,[48] used without modifications as coded in the Gaussian09 suite of programs.[49] The Stuttgart−Dresden ECP pseudopotential and basis set were employed for Ni,[50] which accounts for 18 valence electrons. For all the other atoms the D95V(d) basis set was adopted.[51] This level of theory was already used to predict properties of other β-diketonate−TMEDA compounds,[32,36,52] including the molecular structure of Ni(tfa)$_2$TMEDA, Ni(fod)$_2$TMEDA, and Ni(thd)$_2$TMEDA in the absence of water molecules.[37] Binding energies *per* water molecule (W_{BE}) for the formation of hydrated precursors were calculated adopting the formula

$$W_{BE} = -\frac{E(\mathrm{Ni(L)_2TMEDA}\cdot n(\mathrm{H_2O})) - E(\mathrm{Ni(L)_2TMEDA}) - n\cdot E(\mathrm{H_2O})}{n} \quad (1)$$

with L = tfa, fod, and thd and n = number of water molecules. The zero-point-energy (ZPE) correction was taken into account in calculating water binding energies.

All calculations were performed with the Gaussian 09 code.[49]

Additional details on material synthesis and characterization and theoretical calculations are reported in the Supporting Information.

3. RESULTS AND DISCUSSION

The use of wet oxygen atmospheres produced films featuring mirror-like surfaces, with a homogeneous appearance over the whole area (Figure 2, left panel) and well adherent to the substrates, as indicated by the scotch tape test.

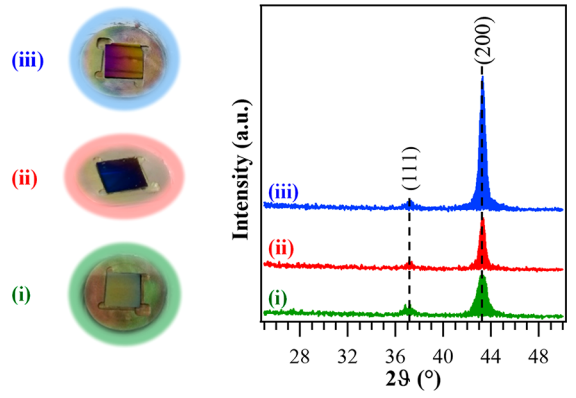

Figure 2. Left panel: digital photographs of films grown on Si(100) from Ni(tfa)$_2$TMEDA (i), Ni(fod)$_2$TMEDA (ii), and Ni(thd)$_2$TMEDA (iii). Right panel: corresponding XRD patterns.

XRD analyses were performed in order to investigate the system structure. All the recorded patterns (Figure 2, right panel) displayed two diffraction peaks located at 2θ = 37.2° and 43.3°, related to the (111) and (200) reflections of cubic nickel(II) oxide (*Fm*-3*m* (225) space group; lattice parameter a_0 = 4.177 Å).[53] As can be noted, the observed reflections obeyed selection rules with (*hkl*) Miller indexes being either all odd or all even, consistent with the face-centered cubic (fcc) NiO lattice.[53] The $I_{(200)}/I_{(111)}$ intensity ratio for the deposit obtained from Ni(thd)$_2$TMEDA (Table 1) was appreciably higher than the one of the polycrystalline powder reference. This result suggested the occurrence of a net (100) preferential orientation, as previously reported for NiO films obtained *via* CVD,[10,31,54] layer epitaxy,[27] and sputtering.[22,23,55,56] Such a phenomenon was traced back to the fact that in the NiO crystal structure (100) planes are the most densely packed planes among the ones composed of both Ni^{2+} and O^{2-}, so that the development of a (100) orientation reduces the surface free energy during the growth of NiO films.[31,56,57] In a different way, for Ni(tfa)$_2$TMEDA- and Ni(fod)$_2$TMEDA-derived samples, $I_{(200)}/I_{(111)}$ ratio values were closer and almost equal, respectively, to the one expected for the powder reference (see Table 1 and caption).

The estimated crystallite dimensions (D) were between 10 and 18 nm, indicating the formation of nanostructured systems. In particular, D values were found to progressively decrease upon going from the Ni(thd)$_2$TMEDA-derived sample to the ones obtained from Ni(fod)$_2$TMEDA and Ni(tfa)$_2$TMEDA (Table 1). As can be observed in Figure 2, right panel, this variation was accompanied by an appreciable decrease of the overall diffracted intensity and of the $I_{(200)}/I_{(111)}$ intensity ratio (Table 1).

Basing on compositional results (see SIMS data below), the samples obtained from Ni(tfa)$_2$TMEDA and Ni(fod)$_2$TMEDA are characterized by fluorine presence. This evidence, in conjunction with the above structural features, suggests that under the adopted preparative conditions F introduction in the NiO network yielded a crystallinity deterioration. Such a result, in line with the ones for F-doped NiO films produced by spray deposition,[39] was accompanied by a progressive loss of the (100) preferred orientation upon increasing the fluorination degree (see also SIMS results), *i.e.*, upon passing from the Ni(tfa)$_2$TMEDA- to the Ni(fod)$_2$TMEDA-derived specimens.

The decrease of crystallite sizes D for the two latter F-containing samples in comparison to the Ni(thd)$_2$TMEDA-derived sample, along with the above variations, can be explained considering that F, rather than substituting for O, is incorporated at grain boundaries, and hence the number of nucleation centers is reduced. These conclusions are also in line with the absence of any appreciable diffraction peak shift, in accordance with the findings reported by Kerli and Alver.[39] The incorporation of F at the grain boundaries is also likely to result in a variation of the relative (200)/(111) surface energies, thus accounting for the observed switch from (100) to (111) growth.

The dislocation density (δ) and microstrain (ε) values for the present materials (calculated as specified in Section S2.1 of the Supporting Information) are reported in Table 1. For comparison purposes, δ and ε values previously obtained in selected studies on NiO films prepared by different techniques are reported in Table S1. As can be observed, δ and ε values are directly dependent not only on the preparation route, but even on the adopted processing conditions. In line with

https://doi.org/10.1021/acs.jpcc.3c05067
J. Phys. Chem. C XXXX, XXX, XXX−XXX

Table 1. Relevant Properties for NiO Nanodeposits Obtained on Si(100) under O_2 + H_2O Atmospheres (D = Average Crystallite Dimensions, δ = Dislocation Density, and ε = Microstrain)

precursor	thickness (nm)	growth rate (nm min^{-1})	$I_{(200)}/I_{(111)}$[a]	D (nm)	δ (lines m^{-2})	ε
Ni(tfa)$_2$TMEDA (i)	180 ± 6	1.46	2.3	10 ± 1	1.0 × 10^{16}	0.560
Ni(fod)$_2$TMEDA (ii)	90 ± 4	0.80	1.8	14 ± 2	5.1 × 10^{15}	0.393
Ni(thd)$_2$TMEDA (iii)	170 ± 6	1.42	12.2	18 ± 2	3.1 × 10^{15}	0.333

[a]The $I_{(200)}/I_{(111)}$ value estimated from the reference powder spectrum is 1.6.[53]

literature data,[19,55,58] in this study lower δ and ε values corresponded to higher crystallite dimensions, *i.e.*, were found for the fluorine-free Ni(thd)$_2$TMEDA-derived nanodeposit (see Table 1). Overall, coherently with SIMS data (see below), these results indicate that fluorine introduction into the deposits obtained from Ni(tfa)$_2$TMEDA and Ni(fod)$_2$TMEDA results in the formation of a higher number of defects. In a different way, the fluorine-free Ni(thd)$_2$TMEDA precursor yields materials featuring a higher crystallinity and enhanced (100) texturing, accompanied by lower dislocation density and microstrain values.

The surface chemical composition of the fabricated deposits was analyzed using XPS. Survey spectra (Figure 3a) displayed

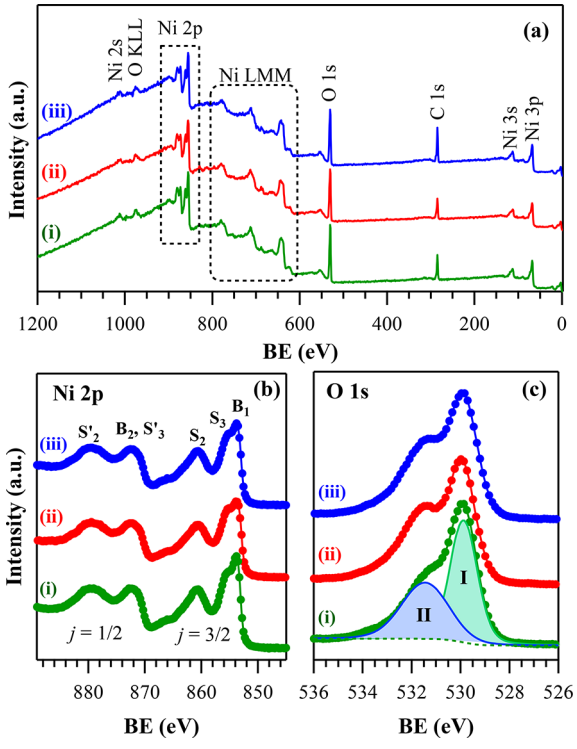

Figure 3. XPS analysis of nickel oxide samples obtained from Ni(tfa)$_2$TMEDA (i), Ni(fod)$_2$TMEDA (ii), and Ni(thd)$_2$TMEDA (iii): (a) wide-scan spectra; (b) Ni 2p and (c) O 1s signals. As an example, in case (i) O 1s fitting components are plotted together with the raw spectrum (**I**: lattice O in Ni(II) oxide; **II**: −OH groups chemisorbed on oxygen defects).

the presence of C (see also Figure S1 and related comments) and Ni and O as major elements. The overall Ni 2p photoelectron peak, possessing an analogous shape and position for all the investigated specimens (Figure 3b), can be roughly divided into two edges split by spin−orbit coupling, referred to as the 2p$_{3/2}$ [features located at 853.8 eV (**B$_1$**), 855.3 eV (**S$_3$**), and 860.7 eV (**S$_2$**)] and 2p$_{1/2}$ [main features at 872.0 eV (**B$_2$** and **S′$_3$**), partially overlapped, and 879.4 eV (**S′$_2$**)] components. The exact attribution of these features, whose positions and shapes are in line with previous data for NiO,[8,18,24,59−61] has so far led to disagreeing interpretations. In fact, various investigators have related the satellite structures at BEs ≈1.5 eV higher with respect to the main peaks (**S$_3$** and **S′$_3$**) to the presence of Ni(III) centers[9,13,14,19,20,62] or to Ni_2O_3.[14,28,54,62] Nevertheless, the presence of these spectral features even for freshly cleaved NiO single crystals indicates that the observed peak shape, typical for NiO,[24,60] likely arises from a contribution of oxygen electronic states, rather than from variations of Ni valence.[59]

Following one of the proposed explanations for the Ni 2p peak shape in the NiO [Ni(II) electronic configuration: 3d^8], the generation of a Ni 2p core level hole results in a significant Coulomb repulsion with 3d holes. Whereas the ground state is endowed with a predominant 3d^8 character, the lowest energy state will then be $c3d^9\underline{O}$ (c and $\underline{O}$: hole in the 2p level and the O band, respectively, **B$_1$** and **B$_2$** peaks in Figure 3b[61]), and the **S$_2$** and **S′$_2$** features can be assigned to unscreened $c3d^8$ final states.[61] Yet, this model fails in explaining the presence **S$_3$** and **S′$_3$** structures at BEs ≈1.5 eV higher than the main lines in both 2p$_{3/2}$ and 2p$_{1/2}$ edges. According to another study, the Ni 2p line shape is significantly affected not only by nearest neighbors but also by next-nearest neighbors,[24] so that a core hole can also be screened by an electron from an adjacent NiO_6 unit. This *nonlocal* screening mechanism also explains the occurrence of literature debates, because the satellite intensity is very sensitive to the adopted preparation route, which, in turn, directly influences material defectivity and crystallinity. On this basis, **S$_3$** and **S′$_3$** features originate from screening by an electron coming from an adjacent NiO_6 unit with respect to the Ni center bearing the core hole. In brief, after the creation of a core hole ($3d^8 \rightarrow c3d^8$), screening electrons from neighboring sites contribute to lowering the system energy ($c3d^8 \rightarrow c3d^9\underline{O}$). Following the above mechanism, an electron is transferred from a neighboring NiO_6 unit ($c3d^8,3d^8 \rightarrow c3d^9,3d^8\underline{O}$). As a result, the emitting Ni site configuration is predominantly $2p^53d^9$,[60] and an additional hole $3d^8\underline{O}$ in an adjacent unit is present.

The O 1s signal (Figure 3c) was deconvoluted by means of a principal component at BE = 529.9 eV (**I**), related to lattice oxygen in NiO,[10,19,20,24,30,60] and a second band at BE = 531.5 eV (**II**), mainly attributable to hydroxyl species chemisorbed on O defects.[16,18,41−43] Consequently, the O/Ni atomic percentage ratio (average value = 1.2) turned out to be slightly higher than the stoichiometric ones expected for NiO. The weight of component **II** corresponded to 52, 54, and 43% of the overall O 1s signal for samples obtained from Ni(tfa)$_2$TMEDA (i), Ni(fod)$_2$TMEDA (ii), and Ni(thd)$_2$TMEDA, respectively. These data suggest that the fluorine presence resulted in a higher defect content in the obtained specimens.

https://doi.org/10.1021/acs.jpcc.3c05067
J. Phys. Chem. C XXXX, XXX, XXX−XXX

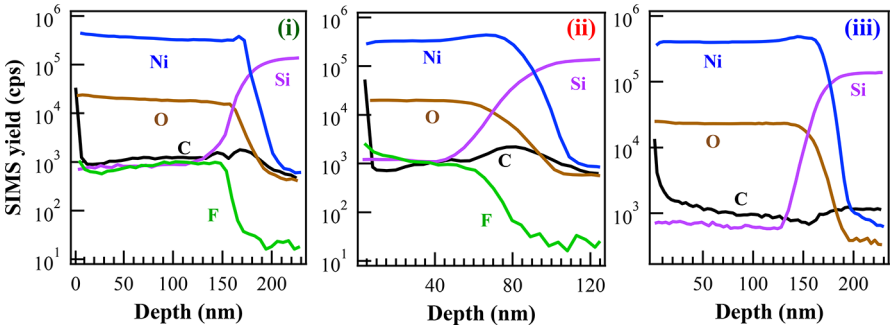

Figure 4. SIMS depth profiles for deposits grown from Ni(tfa)$_2$TMEDA (i), Ni(fod)$_2$TMEDA (ii), and Ni(thd)$_2$TMEDA (iii).

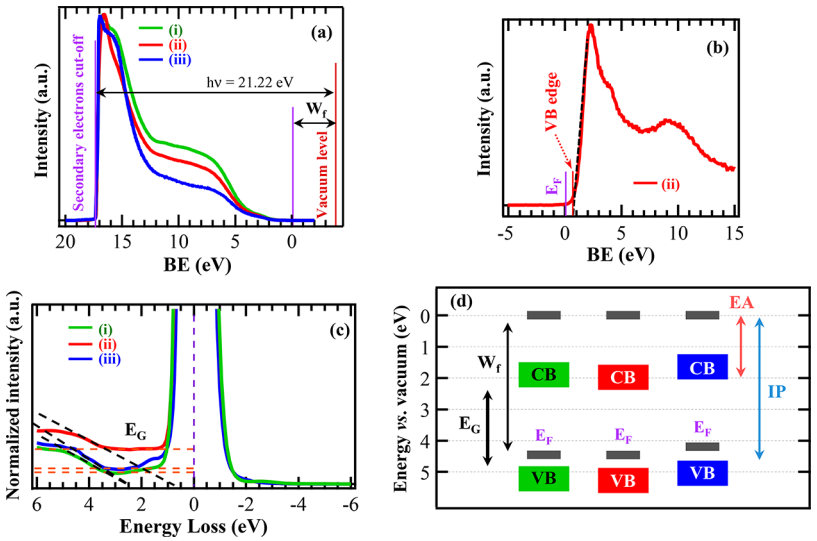

Figure 5. UPS and REELS characterization of samples obtained from Ni(tfa)$_2$TMEDA (i), Ni(fod)$_2$TMEDA (ii), and Ni(thd)$_2$TMEDA (iii). (a) He(I) UPS valence bands. (b) XPS valence band for a NiO specimen grown from Ni(fod)$_2$TMEDA. (c) REELS spectra and (d) energy level positions for the different specimens with respect to the vacuum level (E_F = Fermi level energy; E_G = band gap; W_f = work function; CB = conduction band; VB = valence band; IP = ionization potential; EA = electron affinity).

SIMS measurements (Figure 4) yielded complementary insight into the in-depth film composition as a function of the adopted Ni precursor. As a general rule, carbon signal was higher at the surface and subsequently depleting in the inner specimen regions, thus indicating its adventitious nature. The average C content in the analyzed samples was evaluated to be as low as tenths of ppm, indicating a clean conversion of all the used molecular sources into NiO under the adopted conditions. All the investigated specimens exhibited a well-defined interface with the Si substrate and an even nickel and oxygen distribution throughout their thickness. For deposits obtained from fluorinated compounds [Ni(tfa)$_2$TMEDA and Ni(fod)$_2$TMEDA; Figures 4i and 4ii, respectively], a rather uniform fluorine distribution throughout film thickness was observed, and the almost parallel trends of O, Ni, and F yields suggested a homogeneous system composition. These data, analogous to those obtained for Mn_3O_4,[42] MnO_2,[41] and Fe_2O_3[43] deposits fabricated starting from ML$_2$TMEDA derivatives (M = Mn, Fe; L = tfa, hfa, with Hhfa = 1,1,1,5,5,5-hexafluoro-2,4-pentanedione), confirm that Ni(tfa)$_2$TMEDA and Ni(fod)$_2$TMEDA can successfully act as single-source precursors for the obtainment of F-doped NiO. Upon passing from Ni(tfa)$_2$TMEDA to Ni(fod)$_2$TMEDA-derived deposits, the average fluorine content was estimated to increase from 160 to 650 ppm, according to a reference standard. This variation, perfectly in line with the higher fluorination degree of the fod derivative with respect to the tfa one, indicates the possibility of modulating the fluorine content in the target materials by a simple variation of the adopted Ni precursor, an important issue to tailor the system properties influenced by the dopant concentration. Conversely, no F was detected in the deposit obtained from fluorine-free Ni(thd)$_2$TMEDA, as expected (Figure 4iii).

Additional important information on the properties of the deposited NiO films, as well as on the effect exerted by the different precursors on the work function, band edge position, and band gap value, was obtained by XPS/UPS valence band analyses and REELS measurements. Figure 5a reports UPS valence bands of NiO specimens obtained from the three different precursors, whereas the corresponding XPS valence band spectra are displayed in Figures 5b and S2. The obtained data are reported in Table 2, along with ionization potential and electron affinity values (calculated as indicated in the caption) and energy gap values extrapolated from REELS spectra[4] plotted in Figure 5c. Accordingly, a tentative energy level diagram for the materials presented here is presented in Figure 5d. The obtained band gap values are in line with those reported for NiO films obtained by reactive sputtering[1] and solution processing,[45] and lower than those of NiO films obtained by electron beam evaporation[4] and magnetron

https://doi.org/10.1021/acs.jpcc.3c05067
J. Phys. Chem. C XXXX, XXX, XXX−XXX

Table 2. Work Function (W_f, Measured by UPS), Ionization Potential (IP), Electron Affinity (EA), Energy Gap Values (E_G, Determined by REELS), and Valence Band Edges Separation from the Fermi Level (E_F − VB) for Different NiO Specimens Obtained from the Target Precursors[a]

precursor	W_f (eV)	IP (eV)	EA (eV)	E_G (eV)	E_F − VB (eV)
$Ni(tfa)_2TMEDA$ (i)	4.45	5.22	1.82	3.32	0.77
$Ni(fod)_2TMEDA$ (ii)	4.45	5.27	1.97	3.30	0.81
$Ni(thd)_2TMEDA$ (iii)	4.20	5.04	1.64	3.40	0.84

[a] W_f corresponds to $E_F - E_{vacuum}$, whereas IP (EA) are evaluated as the difference between the valence (conduction) band edges (VB and CB, respectively) and vacuum level E_{vacuum}.[45]

sputtering.[3] The tunable band gap energy suggests that the synthesized nanosystems are promising potential candidates for optoelectronic devices, as well as photoelectrodes for water splitting and gas sensors.

As can be observed in Figures 5b and S2, for specimens obtained from $Ni(tfa)_2TMEDA$ and $Ni(fod)_2TMEDA$, fluorine introduction in NiO (see SIMS depth profiles) resulted in an increased W_f (Table 2) and a lower valence band edge.[1] The obtained offset values of valence band edges from the Fermi level (E_F − VB) pointed out, as expected, to a p-type conductivity of all the obtained systems,[1] with a deeper E_F value in the case of F-doped materials. The values reported in Table 2 are in good agreement with a previous study from Ratcliff et al.[45] on solution-processed NiO films, although slightly higher electron affinities/work functions, and lower (E_F − VB) values were measured. For samples obtained from $Ni(fod)_2TMEDA$ and $Ni(tfa)_2TMEDA$, the electron affinity was slightly higher than the usual value for NiO (≈1.7 eV)[1] (see Table 2). The present work function values were lower than those of solution-processed NiO films, either pure or doped with Cs/Cu,[2,5] and of NiO films prepared by oxidation of sputtered Ni ones.[63]

It is known that NiO work function, and, more generally, electrical and optical properties, depend significantly on the adopted deposition and processing conditions.[2,3,11,45] The increased work function of the target materials resulting from fluorine introduction can indeed facilitate an improved hole extraction, of significant interest for an eventual film utilization in solar cells.[2,5,11]

As also reported for other metal oxides, fluorine introduction can induce shifts in the material band gap, affect the recombination between photogenerated charge carriers, and impact the system resistivity, modifying carrier concentration and mobility.[44] In the present case, as can be observed in Table 2, an increasing fluorine content yielded a progressively lower band gap. This phenomenon can be attributed to the presence of defects in the synthesized material, as confirmed by XRD analyses (see above), in line with previous results on F-doped NiO.[40]

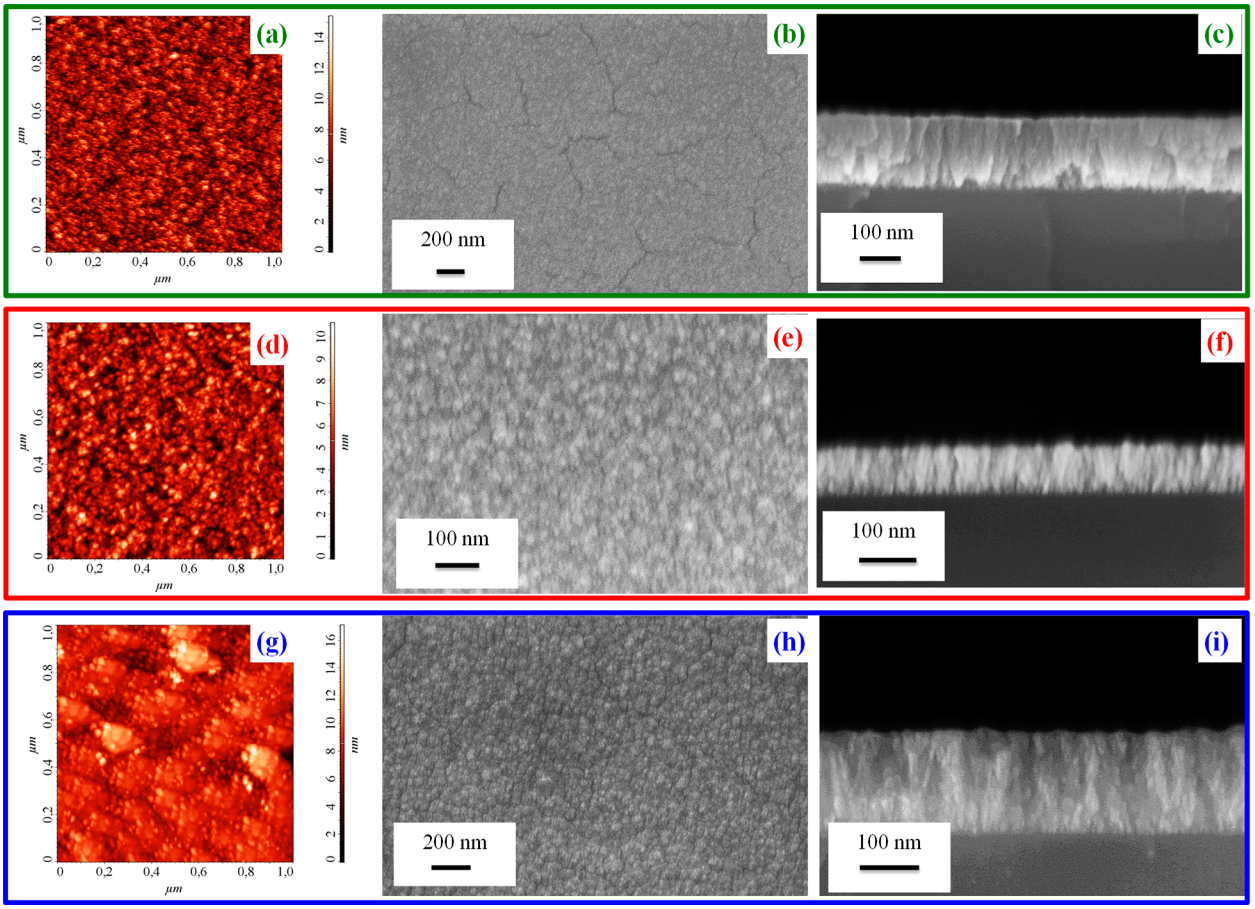

Figure 6. Left to right: representative AFM micrographs, plane-view, and cross-sectional FE-SEM images and for NiO deposits obtained from $Ni(tfa)_2TMEDA$ (a–c), $Ni(fod)_2TMEDA$ (d–f), and $Ni(thd)_2TMEDA$ (g–i).

https://doi.org/10.1021/acs.jpcc.3c05067
J. Phys. Chem. C XXXX, XXX, XXX−XXX

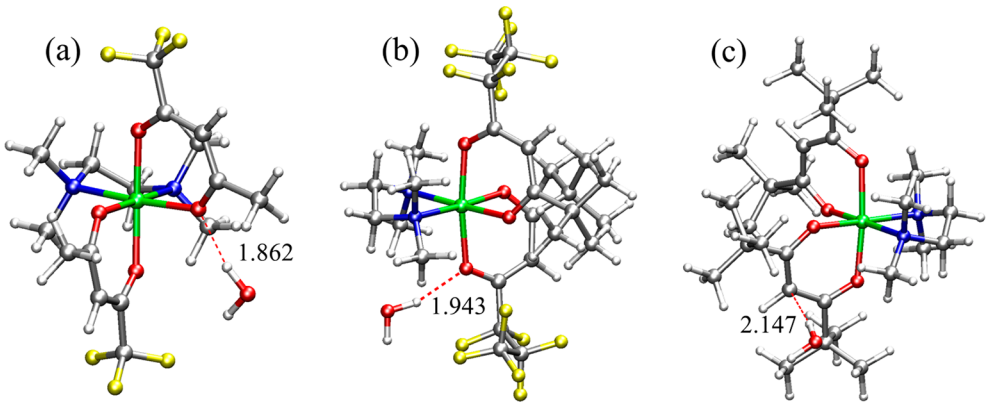

Figure 7. Graphical representation of DFT-calculated optimized structures for hydrated complexes: (a) Ni(tfa)$_2$TMEDA·H$_2$O; (b) Ni(fod)$_2$TMEDA·H$_2$O; and (c) Ni(thd)$_2$TMEDA·H$_2$O. Hydrogen bond distances between a water proton and the complexes are reported in Å. Color codes: Ni, green; F, yellow; O, red; N, blue; C, gray; H, white. The dashed red lines indicate hydrogen bonds in (a) and (b) and the interaction between one H$_2$O proton and the π-system of the diketonate ligands in (c).

Table 3. Average Ni−O and Ni−N Bond Lengths (in Å) and Binding Energy *per* Water Molecule (W_{BE}, kcal mol^{-1}) Computed for the Optimized Geometries of the Dry and Hydrated Complexes

	no water	+ 1 H$_2$O	+ 2 H$_2$O	+ dimer	+ 3 H$_2$O	+ trimer
			Ni(tfa)$_2$TMEDA (i)			
Ni−O ligand 1 (Å)	2.037	2.040	2.040	2.046	2.045	2.051
Ni−O ligand 2 (Å)	2.037	2.036	2.040	2.035	2.039	2.040
Ni−N TMEDA (Å)	2.169	2.167	2.164	2.171	2.167	2.164
W_{BE} (kcal/mol)		9.77	9.14	9.95	9.64	10.14
			Ni(fod)$_2$TMEDA (ii)			
Ni−O ligand 1 (Å)	2.034	2.076	2.087	2.043	2.085	2.040
Ni−O ligand 2 (Å)	2.034	2.044	2.087	2.086	2.095	2.077
Ni−N TMEDA (Å)	2.171	2.156	2.140	2.148	2.135	2.152
W_{BE} (kcal/mol)		6.97	6.85	7.40	7.13	8.08
			Ni(thd)$_2$TMEDA (iii)			
Ni−O ligand 1 (Å)	2.021	2.021	2.024	2.019	2.024	2.019
Ni−O ligand 2 (Å)	2.021	2.025	2.024	2.025	2.024	2.036
Ni−N TMEDA (Å)	2.182	2.176	2.170	2.180	2.174	2.173
W_{BE} (kcal/mol)		7.67	7.37	7.51	7.38	7.44

The system morphology was investigated through the combined use of AFM and FE-SEM analyses (Figure 6). AFM micrographs displayed a uniform topography with relatively flat surfaces, the root-mean-square roughness being 1.3−2.0 nm irrespective of the processing conditions. Plane-view FE-SEM images confirmed a homogeneous coverage of the substrate surface, and the average aggregate dimensions were estimated to be 9 ± 2, 10 ± 4, and 14 ±5 nm for deposits grown from Ni(tfa)$_2$TMEDA, Ni(fod)$_2$TMEDA, and Ni(thd)$_2$TMEDA, respectively. Cross-sectional FE-SEM micrographs unraveled the formation of relatively dense films with well-defined interfaces to the substrate, characterized by the close interconnection of compact columnar structures, observed also for textured (100) NiO films obtained by sputtering.[56] The obtained results evidenced that, under the same operating conditions, experiments from Ni(tfa)$_2$TMEDA and Ni(thd)$_2$TMEDA yielded deposits with almost the same thickness (see Table 1), whereas the use of Ni(fod)$_2$TMEDA precursor yielded thinner films.

The present system morphology can be qualitatively interpreted in the framework of the zone model proposed by Movchan and Demchishin.[64] In the present case, evaluation of the homologous temperature [$T_h = T_{deposition}/T_{melting}$(NiO), with $T_{melting}$(NiO) = 2228 K[65]] yields T_h = 0.302, which corresponds to the formation of columnar aggregates, as indeed observed. Correlation with XRD results indicate that, especially for the sample fabricated from Ni(thd)$_2$TMEDA, this morphology can be associated with the occurrence of a (100) texturing (see the $I_{(200)}/I_{(111)}$ values in Table 1). A comparison of the presently reported results with previous ones[37] clearly highlights that the introduction of water vapor in the reaction atmosphere plays an important role in the obtainment of thicker films, as observed in the CVD of Co_3O_4 from analogous precursors.[34,35]

From thickness data, the maximum growth rate (Table 1) was estimated to be ≈1.4 nm min^{-1} for deposits obtained under O$_2$ + H$_2$O reaction atmospheres starting from Ni(tfa)$_2$TMEDA and Ni(thd)$_2$TMEDA. This value, having the same order of magnitude of those reported in the CVD of NiO from bis(cyclopentadienyl)Ni(II)[62] and nickel bis(1-(dimethylamino)-2-methyl-2-butanolate)[8] and in the PE-CVD of NiO from Ni(II)acetylacetonate,[16] was higher than that reported in the CVD of NiO films from Ni 2-(dimethylamino)-2-methyl-1-propanolate.[10]

To investigate the role of the presence of water vapor in the CVD reaction chamber, the interaction of water molecules with Ni(tfa)$_2$TMEDA, Ni(fod)$_2$TMEDA, and Ni(thd)$_2$TMEDA was modeled using a DFT approach. In

https://doi.org/10.1021/acs.jpcc.3c05067
J. Phys. Chem. C XXXX, XXX, XXX−XXX

particular, variations in the compound molecular geometries and vibrational properties as a function of the number n of water molecules (n = 1−3) in the Ni second coordination shell were examined. We optimized five different structures for each Ni complex: (i) a single H_2O molecule in contact with the complex; (ii) two H_2O molecules located in two different regions of the complex (symmetrically positioned); (iii) a water dimer interacting with the complex; (iv) a water dimer *plus* a single H_2O molecule located in two different regions of the complex; and finally, (v) the interaction of a water trimer with the complex. Graphical representations of the optimized structures calculated for these systems are proposed in Figures S3−S5, whereas relevant geometrical parameters are reported in Tables S2−S4. In all of the cases mentioned above, H_2O molecules were undissociated; however, for the Ni(tfa)$_2$TMEDA complex, an adduct with one dissociated H_2O molecule was considered as well (Figure S6).

As a general observation, H_2O molecules are located in the less sterically hindered regions of the complexes' coordination sphere (see Figures 7 and S3−S5). Water molecules form relatively strong hydrogen bonds with diketonate O atoms in the F-containing ligands.

In a different way, no hydrogen bonds are formed between water molecules and ligand atoms in Ni(thd)$_2$TMEDA, bearing four bulky *tert*-butyl substituents on the diketonate moieties bonded to the Ni center, which prevent H_2O access in the proximity of diketonate O atoms. Nonetheless, water molecules are present in the Ni second coordination shell and interact *via* a proton with the thd diketonate π-structure (see Figures 7c and S5). In Table 3, the average Ni−O and Ni−N distances *per* ligand are reported as a function of the number and the organization of water molecules for each of the three precursors, along with the corresponding binding energies *per* water molecule. A more detailed account of relevant bond distances and angles can be found in Tables S2−S4, while the ZPE contributions are reported in Table S5. Importantly, in all cases, the binding energies *per* water molecule are significantly higher than thermal energy under the adopted CVD conditions (≈1.3 kcal/mol at 400 °C), indicating that the hydrated precursors should be present in the reaction atmosphere during NiO film growth.

Indeed, such findings may shed light on the remarkable rise in the growth rate when water vapor is included in the CVD atmosphere, in comparison to the case of depositions performed under dry O_2. Overall, the water binding energy trend suggests that the effect exerted by water vapor presence should be more pronounced for Ni(tfa)$_2$TMEDA than for Ni(fod)$_2$TMEDA and Ni(thd)$_2$TMEDA. In fact, upon utilizing Ni(tfa)$_2$TMEDA, the film growth rate rises by ≈18 times under O_2 + H_2O reaction atmospheres in comparison to the case of dry O_2, whereas the growth rate increase is comparatively smaller for Ni(fod)$_2$TMEDA (≈10 times) and Ni(thd)$_2$TMEDA (≈5 times).[37] These data highlight that the highest growth rate increase occurs for the precursor capable of being involved in stronger hydrogen bonds with gas-phase water, *i.e.*, Ni(tfa)$_2$TMEDA. Because of the absence of bulky *tert*-butyl groups, Ni(tfa)$_2$TMEDA presents the most sterically favorable environment for a prominent hydrogen bonding of water molecules with diketonate O atoms. In Ni(fod)$_2$TMEDA, containing two *tert*-butyl groups, the formation of (weaker) hydrogen bonds can occur only at the expense of a significant distortion of the Ni coordination sphere. Indeed, the fod containing complex presents the largest water-induced distortion in both Ni−O and Ni−N distances (Tables 3 and S3). As concerns Ni(thd)$_2$TMEDA, even though water molecules cooperate to perturb the Ni coordination environment, thus indirectly influencing Ni−ligand bonding (Tables 3 and S4), the presence of water affects primarily the π-structure of the diketonate. In general, the introduction of H_2O in the Ni second coordination shell induced an elongation of Ni−O bonds for at least one diketonate ligand, whereas Ni−N bonds are always shortened. In spite of water-induced distortions, Ni octahedral coordination environment is maintained in all hydrated complexes. Such an environment undergoes significant changes in the case of dissociated water (Figure S6). Indeed, a highly reactive pentacoordinated structure is predicted in such a case for the Ni(tfa)$_2$TMEDA·$H_2O_{dissociated}$ complex, which presents a protonated TMEDA (at one of the nitrogen atoms) and the transformation of one tfa diketonate into a keto carboxylic acid. However, the water binding energy obtained for this pentacoordinated structure (close to −50 kcal/mol) indicates a very low formation probability in the vapor phase.

Beside geometrical and energetic changes induced by water molecules, we have also performed a vibrational study of the hydrated precursors *via* harmonic frequencies analyses. Particular attention has been devoted to the cases of dihydrated complexes where water is symmetrically positioned close to the diketonate ligands, namely Ni(L)$_2$TMEDA·2H_2O. For these cases, we have performed a thorough analysis of water effects on the modes localized on Ni−O bonds. This choice allows for a more straightforward comparison of the frequencies associated with metal−ligand bonds in the dihydrated complexes with the corresponding values computed for the dry complexes, both characterized by a slightly distorted C_2 symmetry (see the Supporting Information). Stretching frequencies of normal modes principally localized on Ni−O bonds are reported in Tables S6−S8 for both the dry and the symmetrically dihydrated precursors. A careful data inspection reveals that, in line with the previous discussion, the most significant variations are found for Ni(tfa)$_2$TMEDA·2H_2O (Table S6). In particular, despite a frequency increase of collective Ni−O stretching modes, a significant decrease (15 cm^{-1}) in the stretching frequency of modes involving apical Ni−O bonds (*i.e.*, those not in *trans* to the TMEDA ligand), accompanied by an appreciable lengthening of such bonds (Table S2), was computed (Table S6). This result indicates that water plays a key role in weakening two Ni−O bonds, thus significantly perturbing the coordination of tfa ligands to the metal center and likely contributing to activate the precursor decomposition. In the case of Ni(fod)$_2$TMEDA, the stretching frequencies of all modes localized on Ni−O bonds are lowered by the interaction with water (Table S7), but the maximum frequency decrease (10 cm^{-1}) is less pronounced with respect to Ni(tfa)$_2$TMEDA. In a different way, Ni−O stretching frequencies appear to be almost unaffected by the presence of water for Ni(thd)$_2$TMEDA (Table S8). This result can be explained by considering that in this complex water protons interact with the diketonate ligands π-system and, hence, are less effective in weakening Ni interaction with diketonate O atoms. Therefore, while the computed H_2O binding energies suggest that the presence of water vapor should favor the decomposition of all three complexes, the water binding energy trend, along with the decrease of Ni−O bonds' stretching frequencies, indicates that the effect should be more pronounced in the case of Ni(tfa)$_2$TMEDA. These results

https://doi.org/10.1021/acs.jpcc.3c05067
J. Phys. Chem. C XXXX, XXX, XXX−XXX

rationalize why the experimentally determined growth rate is the highest for the films deposited using the $Ni(tfa)_2TMEDA$ precursor and why the impact of water vapor on the growth rate is less significant in the case of the non-fluorinated $Ni(thd)_2TMEDA$ compound. However, also for the $Ni(thd)_2TMEDA$ case, a 5% increase of the growth rate is induced by the introduction of H_2O vapor in the CVD chamber. The analyses of low-energy vibrational modes of the hydrated precursors are useful in order to account for this phenomenon. The calculated IR (harmonic) spectra of the hydrated precursors are reported in Figures S7−S9 and compared with those of nonhydrated ones. For all precursors, the presence of H_2O in the Ni second coordination shell is associated with relatively intense signals below ≈400 cm^{-1}, which are missing in the absence of water. Such signals are primarily due to water libration modes coupled with strong deformation modes of the Ni coordination shell, which might activate precursor fragmentation.[66] Importantly, such modes are thermally accessible at the substrate temperatures adopted in the CVD deposition process (kT at 400 °C corresponds to ≈435 cm^{-1}). Hence, these water-induced deformations of the Ni local environment, present for all three $Ni(L)_2TMEDA$ precursors, might be at the origin of the general water-induced increase in rate growth. This effect is modulated by the nature of the ligands, which determines the extent of water-induced weakening of Ni−O bonds in the three precursors.

4. CONCLUSIONS

In conclusion, this work has proposed a simple single-step CVD route for the obtainment of pure and F-doped NiO films from various Ni(II) β-diketonate−diamine molecular sources featuring a different fluorination degree. A multi-technique characterization by complementary advanced analytical tools, such as UPS and REELS, never applied so far for CVD NiO films, has evidenced the possibility of controlling fluorine doping level as a function of the adopted precursor, a feature enabling a direct modulation of material defect content and electronic properties.

The positive effect exerted by water vapor on the film growth rate was interpreted on the basis of modeling results. These studies revealed that water molecules might form stable adducts with the precursors under the CVD conditions, perturbing the precursor's coordination shell and weakening Ni interaction with the bonded diketonates. The entity of such an effect was found to be directly dependent on the ligand chemical nature.

The fundamental information on the interplay between processing conditions and material characteristics provided by the present work is of key importance for the subsequent investigation and tailoring of the functional behavior. In perspective, the increase in the system work function after fluorine doping is a valuable starting point for possible applications of the present materials as hole extraction layers in solar cells. On the other hand, the modulation of optical and electrical properties resulting from fluorine doping, never reported to date for nickel oxide films obtained by CVD, opens the door to an eventual end-use of the obtained materials as gas sensors and (photo)electrocatalysts. Further efforts will be devoted to NiO film optimization for their technological exploitation, with particular attention to the fabrication of heterostructured systems.

ASSOCIATED CONTENT

Supporting Information

The Supporting Information is available free of charge at https://pubs.acs.org/doi/10.1021/acs.jpcc.3c05067.

Experimental details on material preparation and characterization; XPS and UPS data; supplementary theoretical characterization results (PDF)

AUTHOR INFORMATION

Corresponding Authors

Chiara Maccato − *Department of Chemical Sciences, Padova University and INSTM, 35131 Padova, Italy; CNR-ICMATE and INSTM, Department of Chemical Sciences, Padova University, 35131 Padova, Italy;* orcid.org/0000-0001-6368-5754; Email: chiara.maccato@unipd.it

Gloria Tabacchi − *Department of Science and High Technology, Insubria University and INSTM, 22100 Como, Italy;* orcid.org/0000-0002-1988-6775; Email: gloria.tabacchi@uninsubria.it

Authors

Mattia Benedet − *Department of Chemical Sciences, Padova University and INSTM, 35131 Padova, Italy; CNR-ICMATE and INSTM, Department of Chemical Sciences, Padova University, 35131 Padova, Italy*

Gioele Pagot − *Section of Chemistry for the Technology (ChemTech), Department of Industrial Engineering, Padova University and INSTM, 35131 Padova, Italy;* orcid.org/0000-0002-4015-6670

Cristiano Invernizzi − *Department of Science and High Technology, Insubria University and INSTM, 22100 Como, Italy*

Cinzia Sada − *Department of Physics and Astronomy, Padova University and INSTM, 35131 Padova, Italy;* orcid.org/0000-0002-7607-0481

Vito Di Noto − *Section of Chemistry for the Technology (ChemTech), Department of Industrial Engineering, Padova University and INSTM, 35131 Padova, Italy;* orcid.org/0000-0002-8030-6979

Gian Andrea Rizzi − *Department of Chemical Sciences, Padova University and INSTM, 35131 Padova, Italy; CNR-ICMATE and INSTM, Department of Chemical Sciences, Padova University, 35131 Padova, Italy;* orcid.org/0000-0001-5201-8104

Ettore Fois − *Department of Science and High Technology, Insubria University and INSTM, 22100 Como, Italy;* orcid.org/0000-0002-7170-8458

Davide Barreca − *CNR-ICMATE and INSTM, Department of Chemical Sciences, Padova University, 35131 Padova, Italy;* orcid.org/0000-0002-8779-3386

Complete contact information is available at: https://pubs.acs.org/10.1021/acs.jpcc.3c05067

Notes

The authors declare no competing financial interest.

ACKNOWLEDGMENTS

The authors gratefully acknowledge CNR (Progetti di Ricerca @CNR - avviso 2020 - ASSIST), Padova University (PDiSC#04BIRD2020-UNIPD EUREKA, DOR 2021−2023), INSTM Consortium (INSTM21PDGASPAROTTO - $NANO^{MAT}$, INSTM21PDBARMAC - ATENA), Insubria

University (FAR2021), and PRIN 2022474YE8 (SCI-TRO-PHY project). Many thanks are also due to Prof. Alberto Gasparotto (Department of Chemical Sciences, Padova University) for skillful experimental support, to Prof. M. Sambi (Department of Chemical Sciences, Padova University) for invaluable discussions on XPS data interpretation, and to Dr. D. Canton (Department of Chemical Sciences, Padova University) for technical help.

REFERENCES

(1) Pintor-Monroy, M. I.; Murillo-Borjas, B. L.; Catalano, M.; Quevedo-Lopez, M. A. Controlling Carrier Type and Concentration in NiO Films to Enable *in situ* PN Homojunctions. *ACS Appl. Mater. Interfaces* **2019**, *11*, 27048−27056.

(2) Chen, W.; Liu, F.-Z.; Feng, X.-Y.; Djurišić, A. B.; Chan, W. K.; He, Z.-B. Cesium Doped NiO_x as an Efficient Hole Extraction Layer for Inverted Planar Perovskite Solar Cells. *Adv. Energy Mater.* **2017**, *7*, No. 1700722.

(3) Park, C.; Kim, J.; Lee, K.; Oh, S. K.; Kang, H. J.; Park, N. S. Electronic, Optical and Electrical Properties of Nickel Oxide Thin Films Grown by RF Magnetron Sputtering. *Appl. Sci. Convergence Technol.* **2015**, *24*, 72−76.

(4) Denny, Y. R.; Lee, K.; Park, C.; Oh, S. K.; Kang, H. J.; Yang, D.-S.; Seo, S. Electronic, Electrical and Optical Properties of Undoped and Na-Doped NiO Thin Films. *Thin Solid Films* **2015**, *591*, 255−260.

(5) Chen, W.; Wu, Y.; Fan, J.; Djurisic, A. B.; Liu, F.; Tam, H. W.; Ng, A.; Surya, C.; Chan, W. K.; Wang, D.; He, Z.-B. Understanding the Doping Effect on NiO: Toward High-Performance Inverted Perovskite Solar Cells. *Adv. Energy Mater.* **2018**, *8*, No. 1703519.

(6) Lindahl, E.; Ottosson, M.; Carlsson, J.-O. Atomic Layer Deposition of NiO by the $Ni(thd)_2/H_2O$ Precursor Combination. *Chem. Vap. Deposition* **2009**, *15*, 186−191.

(7) Lindahl, E.; Lu, J.; Ottosson, M.; Carlsson, J. O. Epitaxial NiO (100) and NiO (111) Films Grown by Atomic Layer Deposition. *J. Cryst. Growth* **2009**, *311*, 4082−4088.

(8) Min, K. C.; Kim, M.; You, Y. H.; Lee, S. S.; Lee, Y. K.; Chung, T. M.; Kim, C. G.; Hwang, J. H.; An, K. S.; Lee, N. S.; et al. NiO Thin Films by MOCVD of $Ni(dmamb)_2$ and their Resistance Switching Phenomena. *Surf. Coat. Technol.* **2007**, *201*, 9252−9255.

(9) Tian, J.; Jiang, H.; Zhao, X.; Shi, G.; Dai, Y.; Deng, X.; Xie, H.; Zhang, W. Hydrogen Sensor with ppb-Level Detection Limit Prepared by Pd-Modified and Bi-Doped Oxidized Ni Foam. *Sens. Actuators, B* **2022**, *366*, No. 131981.

(10) Wilson, R. L.; Macdonald, T. J.; Lin, C.-T.; Xu, S.; Taylor, A.; Knapp, C. E.; Guldin, S.; McLachlan, M. A.; Carmalt, C. J.; Blackman, C. S. Chemical Vapour Deposition (CVD) of Nickel Oxide using the Novel Nickel Dialkylaminoalkoxide Precursor $[Ni(dmamp')_2]$ (dmamp′ = 2-dimethylamino-2-methyl-1-propanolate). *RSC Adv.* **2021**, *11*, 22199−22205.

(11) Imran, M.; Coskun, H.; Khan, N. A.; Ouyang, J. Role of Annealing Temperature of Nickel Oxide (NiO_x) as Hole Transport Layer in Work Function Alignment with Perovskite. *Appl. Phys. A: Mater. Sci. Process.* **2021**, *127*, No. 117.

(12) Roffi, T. M.; Nozaki, S.; Uchida, K. Growth Mechanism of Single-Crystalline NiO Thin Films Grown by Metal Organic Chemical Vapor Deposition. *J. Cryst. Growth* **2016**, *451*, 57−64.

(13) Han, S. W.; Kim, I. H.; Kim, D. H.; Park, K. J.; Park, E. J.; Jeong, M.-G.; Kim, Y. D. Temperature Regulated-Chemical Vapor Deposition for Incorporating NiO Nanoparticles into Mesoporous Media. *Appl. Surf. Sci.* **2016**, *385*, 597−604.

(14) Kitchamsetti, N.; Ramteke, M. S.; Rondiya, S. R.; Mulani, S. R.; Patil, M. S.; Cross, R. W.; Dzade, N. Y.; Devan, R. S. DFT and Experimental Investigations on the Photocatalytic Activities of NiO Nanobelts for Removal of Organic Pollutants. *J. Alloys Compd.* **2021**, *855*, No. 157337.

(15) An, W.-J.; Thimsen, E.; Biswas, P. Aerosol-Chemical Vapor Deposition Method For Synthesis of Nanostructured Metal Oxide Thin Films With Controlled Morphology. *J. Phys. Chem. Lett.* **2010**, *1*, 249−253.

(16) Weidler, N.; Schuch, J.; Knaus, F.; Stenner, P.; Hoch, S.; Maljusch, A.; Schäfer, R.; Kaiser, B.; Jaegermann, W. X-ray Photoelectron Spectroscopic Investigation of Plasma-Enhanced Chemical Vapor Deposited NiO_x, $NiO_x(OH)_y$, and $CoNiO_x(OH)_y$: Influence of the Chemical Composition on the Catalytic Activity for the Oxygen Evolution Reaction. *J. Phys. Chem. C* **2017**, *121*, 6455−6463.

(17) Hussain, N.; Yang, W.; Dou, J.; Chen, Y.; Qian, Y.; Xu, L. Ultrathin Mesoporous F-Doped α-$Ni(OH)_2$ Nanosheets as an Efficient Electrode Material for Water Splitting and Supercapacitors. *J. Mater. Chem. A* **2019**, *7*, 9656−9664.

(18) Hemmati, K.; Kumar, A.; Jadhav, A. R.; Moradlou, O.; Moshfegh, A. Z.; Lee, H. Nanorod Array-Based Hierarchical NiO Microspheres as a Bifunctional Electrocatalyst for a Selective and Corrosion-Resistance Seawater Photo/Electrolysis System. *ACS Catal.* **2023**, *13*, 5516−5528.

(19) Salunkhe, P.; A V, M. A.; Kekuda, D. Investigation on Tailoring Physical Properties of Nickel Oxide Thin Films Grown by DC Magnetron Sputtering. *Mater. Res. Express* **2020**, *7*, No. 016427.

(20) Kim, D. S.; Lee, H. C. Nickel Vacancy Behavior in the Electrical Conductance of Nonstoichiometric Nickel Oxide Film. *J. Appl. Phys.* **2012**, *112*, No. 034504.

(21) Ahmed, A. A.; Devarajan, M.; Afzal, N. Effects of Substrate Temperature on the Degradation of RF Sputtered NiO Properties. *Mater. Sci. Semicond. Process.* **2017**, *63*, 137−141.

(22) Elmassi, S.; Narjis, A.; Nkhaili, L.; Elkissani, A.; Amiri, L.; Drissi, S.; Abali, A.; Bousseta, M.; Outzourhit, A. Effect of Annealing on Structural, Optical and Electrical Properties of Nickel Oxide Thin Films synthesized by the Reactive Radio Frequency Sputtering. *Physica B* **2022**, *639*, No. 413980.

(23) Jamal, M. S.; Shahahmadi, S. A.; Chelvanathan, P.; Alharbi, H. F.; Karim, M. R.; Ahmad Dar, M.; Luqman, M.; Alharthi, N. H.; Al-Harthi, Y. S.; Aminuzzaman, M.; et al. Effects of Growth Temperature on the Photovoltaic Properties of RF Sputtered Undoped NiO Thin Films. *Results Phys.* **2019**, *14*, No. 102360.

(24) Alders, D.; Voogt, F. C.; Hibma, T.; Sawatzky, G. A. Nonlocal Screening Effects in 2p X-ray Photoemission Spectroscopy of NiO (100). *Phys. Rev. B* **1996**, *54*, 7716−7719.

(25) Kate, R. S.; Bulakhe, S. C.; Deokate, R. J. Co Doping Effect on Structural and Optical Properties of Nickel Oxide (NiO) Thin Films via Spray Pyrolysis. *Opt. Quantum Electron.* **2019**, *51*, 319.

(26) Utriainen, M.; Kröger-Laukkanen, M.; Johansson, L.-S.; Niinistö, L. Studies of Metallic Thin Film Growth in an Atomic Layer Epitaxy Reactor using $M(acac)_2$ (M = Ni, Cu, Pt) Precursors. *Appl. Surf. Sci.* **2000**, *157*, 151−158.

(27) Utriainen, M.; Kröger-Laukkanen, M.; Niinistö, L. Studies of NiO Thin Film Formation by Atomic Layer Epitaxy. *Mater. Sci. Eng., B* **1998**, *54*, 98−103.

(28) Yang, T. S.; Cho, W.; Kim, M.; An, K.-S.; Chung, T.-M.; Kim, C. G.; Kim, Y. Atomic Layer Deposition of Nickel Oxide Films using $Ni(dmamp)_2$ and Water. *J. Vac. Sci. Technol., A* **2005**, *23*, 1238−1243.

(29) Zhang, Y.; Du, L.; Liu, X.; Ding, Y. High Growth per Cycle Thermal Atomic Layer Deposition of Ni Films using an Electron-Rich Precursor. *Nanoscale* **2019**, *11*, 3484−3488.

(30) Basato, M.; Faggin, E.; Tubaro, C.; Veronese, A. C. Volatile Square Planar β-Imino Carbonyl Enolato Complexes of Pd(II) and Ni(II) as Potential MOCVD Precursors. *Polyhedron* **2009**, *28*, 1229−1234.

(31) Chandrakala, M.; Raj Bharath, S.; Maiyalagan, T.; Arockiasamy, S. Synthesis, Crystal Structure and Vapour Pressure Studies of Novel Nickel Complex as Precursor for NiO Coating by Metalorganic Chemical Vapour Deposition Technique. *Mater. Chem. Phys.* **2017**, *201*, 344−353.

(32) Maccato, C.; Bigiani, L.; Carraro, G.; Gasparotto, A.; Seraglia, R.; Kim, J.; Devi, A.; Tabacchi, G.; Fois, E.; Pace, G.; Di Noto, V.; Barreca, D. Molecular Engineering of Mn^{II} Diamine Diketonate

https://doi.org/10.1021/acs.jpcc.3c05067
J. Phys. Chem. C XXXX, XXX, XXX−XXX

Precursors for the Vapor Deposition of Manganese Oxide Nanostructures. *Chem.—Eur. J.* **2017**, *23*, 17954−17963.
(33) Barreca, D.; Bigiani, L.; Klotzsche, M.; Gasparotto, A.; Seraglia, R.; Jandl, C.; Pöthig, A.; Fois, E.; Vanin, L.; Tabacchi, G.; et al. A Versatile Fe(II) Diketonate Diamine Adduct: Preparation, Characterization and Validation in the Chemical Vapor Deposition of Iron Oxide Nanomaterials. *Mater. Chem. Phys.* **2022**, *277*, No. 125534.
(34) Barreca, D.; Gasparotto, A.; Lebedev, O. I.; Maccato, C.; Pozza, A.; Tondello, E.; Turner, S.; Van Tendeloo, G. Controlled Vapor-Phase Synthesis of Cobalt Oxide Nanomaterials with Tuned Composition and Spatial Organization. *CrystEngComm* **2010**, *12*, 2185−2197.
(35) Klotzsche, M.; Barreca, D.; Bigiani, L.; Seraglia, R.; Gasparotto, A.; Vanin, L.; Jandl, C.; Pöthig, A.; Roverso, M.; Bogialli, S.; et al. Facile Preparation of a Cobalt Diamine Diketonate Adduct as a Potential Vapor Phase Precursor for Co_3O_4 Films. *Dalton Trans.* **2021**, *50*, 10374−10385.
(36) Tabacchi, G.; Fois, E.; Barreca, D.; Gasparotto, A. CVD Precursors for Transition Metal Oxide Nanostructures: Molecular Properties, Surface Behavior and Temperature Effects. *Phys. Status Solidi A* **2014**, *211*, 251−259.
(37) Benedet, M.; Barreca, D.; Fois, E.; Seraglia, R.; Tabacchi, G.; Roverso, M.; Pagot, G.; Invernizzi, C.; Gasparotto, A.; Heidecker, A. A.; et al. Interplay between Coordination Sphere Engineering and Properties of Nickel Diketonate-Diamine Complexes as Vapor Phase Precursors for the Growth of NiO Thin Films. *Dalton Trans.* **2023**, *52*, 10677−10688.
(38) Fragoso, J.; Barreca, D.; Bigiani, L.; Gasparotto, A.; Sada, C.; Lebedev, O. I.; Modin, E.; Pavlovic, I.; Sánchez, L.; Maccato, C. Enhanced Photocatalytic Removal of NO_x Gases by β-Fe_2O_3/CuO and β-Fe_2O_3/WO_3 Nanoheterostructures. *Chem. Eng. J.* **2022**, *430*, No. 132757.
(39) Kerli, S.; Alver, U. Effect of F-Doping on Structural, Electrical, and Optical Properties of NiO Thin Films. *Crystallogr. Rep.* **2014**, *59*, 1103−1106.
(40) Singh, K.; Kumar, M.; Singh, D.; Singh, M.; Singh, P.; Singh, B.; Kaur, G.; Bala, R.; Thakur, A.; Kumar, A. Fluorine-Doped NiO Nanostructures: Structural, Morphological and Spectroscopic Studies. *AIP Conf. Proc.* **2018**, *1953*, No. 030219.
(41) Barreca, D.; Carraro, G.; Fois, E.; Gasparotto, A.; Gri, F.; Seraglia, R.; Wilken, M.; Venzo, A.; Devi, A.; Tabacchi, G.; et al. Manganese(II) Molecular Sources for Plasma-Assisted CVD of Mn Oxides and Fluorides: From Precursors to Growth Process. *J. Phys. Chem. C* **2018**, *122*, 1367−1375.
(42) Bigiani, L.; Barreca, D.; Gasparotto, A.; Sada, C.; Martí-Sanchez, S.; Arbiol, J.; Maccato, C. Controllable Vapor Phase Fabrication of F:Mn_3O_4 Thin Films Functionalized with Ag and TiO_2. *CrystEngComm* **2018**, *20*, 3016−3024.
(43) Carraro, G.; Barreca, D.; Bekermann, D.; Montini, T.; Gasparotto, A.; Gombac, V.; Maccato, C.; Fornasiero, P. Supported F-Doped α-Fe_2O_3 Nanomaterials: Synthesis, Characterization and Photo-Assisted H_2 Production. *J. Nanosci. Nanotechnol.* **2013**, *13*, 4962−4968.
(44) Carraro, G.; Gasparotto, A.; Maccato, C.; Bontempi, E.; Lebedev, O. I.; Sada, C.; Turner, S.; Van Tendeloo, G.; Barreca, D. Rational Synthesis of F-doped Iron Oxides on Al_2O_3(0001) Single Crystals. *RSC Adv.* **2014**, *4*, 52140−52146.
(45) Ratcliff, E. L.; Meyer, J.; Steirer, K. X.; Garcia, A.; Berry, J. J.; Ginley, D. S.; Olson, D. C.; Kahn, A.; Armstrong, N. R. Evidence for Near-Surface NiOOH Species in Solution-Processed NiO_x Selective Interlayer Materials: Impact on Energetics and the Performance of Polymer Bulk Heterojunction Photovoltaics. *Chem. Mater.* **2011**, *23*, 4988−5000.
(46) Helander, M. G.; Greiner, M. T.; Wang, Z. B.; Lu, Z. H. Pitfalls in Measuring Work Function Using Photoelectron Spectroscopy. *Appl. Surf. Sci.* **2010**, *256*, 2602−2605.
(47) https://imagej.net/ij/index.html (accessed February 2023).
(48) Chai, J.-D.; Head-Gordon, M. Long-range Corrected Hybrid Density Functionals with Damped Atom−Atom Dispersion Corrections. *Phys. Chem. Chem. Phys.* **2008**, *10*, 6615−6620.
(49) Frisch, M. J.; Trucks, G. W.; Schlegel, H. B.; Scuseria, G. E.; Robb, M. A.; Cheeseman, J. R.; Scalmani, J.; Barone, V.; Mennucci, B.; Petersson, G. A.; et al. *GAUSSIAN 09 (Revision B.01)*; Gaussian, Inc.: Wallingford, CT.
(50) Bergner, A.; Dolg, M.; Küchle, W.; Stoll, H.; Preuß, H. Ab initio Energy-Adjusted Pseudopotentials for Elements of Groups 13−17. *Mol. Phys.* **1993**, *80*, 1431−1441.
(51) Dunning, T. H.; Hay, P. J. In *Modern Theoretical Chemistry*; Plenum: New York, 1976; Vol. *2*, Chapter 1.
(52) Barreca, D.; Fois, E.; Gasparotto, A.; Maccato, C.; Oriani, M.; Tabacchi, G. The Early Steps of Molecule-to-Material Conversion in Chemical Vapor Deposition (CVD): A Case Study. *Molecules* **2021**, *26*, 1988.
(53) Pattern no. 00-0047-1049, JCPDS, 2000.
(54) Kang, J.-K.; Rhee, S.-W. Chemical Vapor Deposition of Nickel Oxide Films from $Ni(C_5H_5)_2/O_2$. *Thin Solid Films* **2001**, *391*, 57−61.
(55) Ahmed, A. A.; Afzal, N.; Devarajan, M.; Subramani, S. Structural, Morphological, Optical and Electrical Properties of NiO Films Prepared on Si(100) and Glass Substrates at Different Thicknesses. *Mater. Res. Express* **2016**, *3*, No. 116405.
(56) Ryu, H.-W.; Choi, G.-P.; Hong, G.-J.; Park, J.-S. Growth and Surface Morphology of Textured NiO Thin Films Deposited by Off-Axis RF Magnetron Sputtering. *Jpn. J. Appl. Phys.* **2004**, *43*, 5524.
(57) Fujii, E.; Tomozawa, A.; Torii, H.; Takayama, R. Preferred Orientations of NiO Films Prepared by Plasma-Enhanced Metal-organic Chemical Vapor Deposition. *Jpn. J. Appl. Phys.* **1996**, *35*, L328−L330.
(58) Hajakbari, F. Characterization of Nanocrystalline Nickel Oxide Thin Films Prepared at Different Thermal Oxidation Temperatures. *J. Nanostruct. Chem.* **2020**, *10*, 97−103.
(59) Nesbitt, H. W.; Legrand, D.; Bancroft, G. M. Interpretation of Ni2p XPS Spectra of Ni Conductors and Ni Insulators. *Phys. Chem. Miner.* **2000**, *27*, 357−366.
(60) Altieri, S.; Tjeng, L. H.; Tanaka, A.; Sawatzky, G. A. Core-Level X-ray Photoemission on NiO in the Impurity Limit. *Phys. Rev. B* **2000**, *61*, 13403−13409.
(61) D'Addato, S.; Grillo, V.; Altieri, S.; Tondi, R.; Valeri, S.; Frabboni, S. Structure and Stability of Nickel/Nickel Oxide Core−Shell Nanoparticles. *J. Phys.: Condens. Matter* **2011**, *23*, No. 175003.
(62) Yeh, W.-c.; Matsumura, M. Chemical Vapor Deposition of Nickel Oxide Films from Bis-π-Cyclopentadienyl-Nickel. *Jpn. J. Appl. Phys.* **1997**, *36*, 6884−6887.
(63) Greiner, M. T.; Helander, M. G.; Wang, Z.-B.; Tang, W.-M.; Lu, Z.-H. Effects of Processing Conditions on the Work Function and Energy-Level Alignment of NiO Thin Films. *J. Phys. Chem. C* **2010**, *114*, 19777−19781.
(64) Wahl, G. Protective Coatings. In *Chemical Vapor Deposition - Principles and Applications*; Hitchman, M. L., Jensen, K. F.,, Eds.; Academic Press: London, 1993; pp 598−600.
(65) Lide, D. R., Ed.; *CRC Handbook of Chemistry and Physics*; CRC Press: Boca Raton, FL, 2005.
(66) Fois, E.; Tabacchi, G.; Barreca, D.; Gasparotto, A.; Tondello, E. Hot Surface Activation of Molecular Complexes: Insight from Modeling Studies. *Angew. Chem., Int. Ed.* **2010**, *49*, 1944−1948.

https://doi.org/10.1021/acs.jpcc.3c05067
J. Phys. Chem. C XXXX, XXX, XXX−XXX